J. Fluid Mech. (2007), *vol.* 592, *pp.* 221–231.
doi:10.1017/S0022112007008610 Printed in the United Kingdom

Effects of Prandtl number and a new instability mode in a plane thermal plume

R. LAKKARAJU AND MEHEBOOB ALAM†

Engineering Mechanics Unit, Jawaharlal Nehru Center for Advanced Scientific Research, Jakkur PO, Bangalore 560064, India

(Received 1 July 2007 and in revised form 10 September 2007)

The effect of Prandtl number on the linear stability of a plane thermal plume is analysed under quasi-parallel approximation. At large Prandtl numbers ($Pr > 100$), we found that there is an additional unstable loop whose size increases with increasing Pr. The origin of this new instability mode is shown to be tied to the coupling of the momentum and thermal perturbation equations. Analyses of the perturbation kinetic energy and thermal energy suggest that the buoyancy force is the main source of perturbation energy at high Prandtl numbers that drives this instability.

1. Introduction

The classic problem of natural-convection flow above a horizontal line heat source has received considerable attention during the last few decades (Batchelor 1954; Fujii 1963; Gebhart *et al.* 1988). The temperature of the heat source is greater than that of the ambient fluid, and the resulting density difference creates a plume that rises up against gravity. For steady laminar plumes, the similarity solutions of the pertinent boundary-layer equations have been published by many workers (Fujii 1963; Gebhart, Pera & Schorr 1970; Riley 1974); experimental studies on laminar plane plumes are in good agreement with similarity solutions (Riley 1974). Experiments (Pera & Gebhart 1971) have confirmed that the laminar plumes are unstable, and they sway in a plane perpendicular to the axis of the source. Pera & Gebhart (1971) have shown that the initial instability of plane plumes to two-dimensional disturbances can be analysed by the linear stability theory and developed the coupled Orr–Sommerfeld type equations using a quasi-parallel flow approximation. Since Squire's theorem holds for natural convection flows (Gebhart *et al.* 1988), it is sufficient to consider two-dimensional disturbances for the stability analysis of a thermal plume.

Strictly speaking, the thermal plume is a non-parallel flow field, and the streamwise variations of both the laminar and disturbed flows should be incorporated in the stability analysis (Hieber & Nash 1975; Wakitani 1985). From a weakly non-parallel spatial stability analysis (Wakitani 1985), it has been shown that the critical Grashof number of a plane thermal plume is slightly larger than that predicted from the quasi-parallel theory, even though its precise value depends on the flow quantity (fluctuating kinetic energy or thermal energy, etc.) that is being monitored to calculate non-parallel corrections. It was shown that a lower branch of the neutral stability curve in the (frequency, Grashof number)-plane exists when the non-parallel corrections are taken

† Author to whom correspondence should be addressed: meheboob@jncasr.ac.in

into account. The upper branch of the neutral curve at moderate-to-large values of Grashof number remains relatively unaffected, however, with non-parallel corrections.

Two non-dimensional numbers involved in natural convection phenomena are the Grashof number (Gr), the ratio of the buoyancy force and the viscous force, and the Prandtl number (Pr), the ratio of the kinematic viscosity and the thermal diffusivity. In terms of Pr, there are two limiting cases: the zero-Prandtl-number limit (e.g. molten metals $Pr \sim 10^{-2}$) and the infinite-Prandtl-number limit (e.g. $Pr \sim 10^3$ for magmas, and $Pr \sim 10^{21}$ for the Earth's mantle plume). Geological flows involve fluids with large Prandtl numbers (Worster 1985; Lister 1987; Grossman & Lohse 2000; Kaminski & Jaupert 2003; Majumder, Yuen & Vincent 2004) and are studied in the limit of infinite Prandtl number (Wang 2004) for which the inertial terms in the momentum equations are neglected.

The goal of the present work is to understand the stability characteristics of high-Prandtl-number plane thermal plumes. To the best of our knowledge, all stability analyses of plane thermal plumes (Pera & Gebhart 1971; Hieber & Nash 1975; Wakitani 1985) are confined to that of air ($Pr = 0.7$) and water ($Pr = 6.7$). We use the quasi-parallel approximation to analyse the linear stability of a thermal plume which is found to be unstable for very small Grashof numbers at any Prandtl number. At high Prandtl numbers, we find a new instability loop which is shown to be tied to the coupling of the hydrodynamic and thermal perturbation equations. An analysis of the perturbation energy unveils the driving mechanism of this instability.

2. Governing equations and base flow

We consider the convective flow generated above a line heat source in an otherwise stagnant fluid which is maintained at a constant temperature T_∞. Let the Cartesian coordinate system be (x, y), with x being directed along the flow direction (i.e. against gravity) and y the transverse direction, and u and v are the corresponding velocity components along the x- and y-directions, respectively, and t is the time. With Boussinesq approximation, the governing equations for the velocity and the temperature fields are given by

$$\frac{\partial u}{\partial t} + u\frac{\partial u}{\partial x} + v\frac{\partial u}{\partial y} = \nu\nabla^2 u - \frac{1}{\rho}\frac{\partial p}{\partial x} + g\beta(T - T_\infty), \tag{2.1}$$

$$\frac{\partial v}{\partial t} + u\frac{\partial v}{\partial x} + v\frac{\partial v}{\partial y} = \nu\nabla^2 v - \frac{1}{\rho}\frac{\partial p}{\partial y}, \tag{2.2}$$

$$\frac{\partial T}{\partial t} + u\frac{\partial T}{\partial x} + v\frac{\partial T}{\partial y} = \kappa\nabla^2 T, \qquad \frac{\partial u}{\partial x} + \frac{\partial v}{\partial y} = 0. \tag{2.3}$$

Here ρ is the mean density of the fluid, p is the pressure and g is the acceleration due to gravity; the thermo-physical properties of the fluid are the thermal expansion coefficient β, the kinematic viscosity ν, the thermal conductivity k, the specific heat at constant pressure c_p and the thermal diffusivity $\kappa = k/\rho c_p$. The boundary conditions on velocity and temperature are: $u = v = 0$, $T = T_s$ at $x = y = 0$ and $u = v = T = 0$ at $x^2 + y^2 \to \infty$.

2.1. *Base flow: similarity solution*

The steady laminar base flow is given by the leading-order boundary-layer equations (Fujii 1963; Gebhart *et al.* 1970; Pera & Gebhart 1971; Riley 1974) that can be expressed in terms of a streamfunction: $u = \partial\psi/\partial y$, $v = -\partial\psi/\partial x$. The resulting partial differential equations (not shown) can be transformed into a set of ODEs in

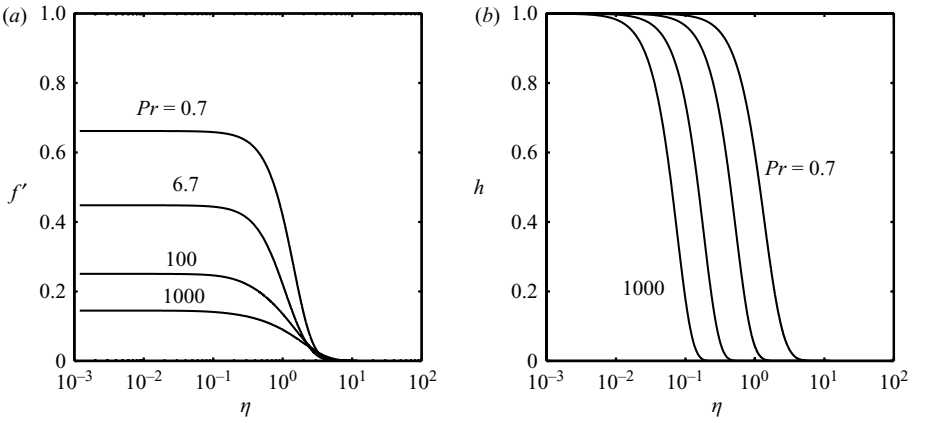

FIGURE 1. Variations of the base-state (*a*) velocity (f') and (*b*) temperature (h) with Prandtl number.

terms of a similarity variable $\eta = y/\delta$, with $\delta = 4x/G$, where

$$Gr = \frac{g\beta(T_0(x) - T_\infty)x^3}{\nu^2}, \quad G = 4\left(\frac{Gr}{4}\right)^{1/4}, \tag{2.4}$$

are the local Grashof number and the 'modified' Grashof number, respectively, and $T_0(x) \equiv T(x, y = 0)$ is the local centreline temperature. The non-dimensional streamfunction and temperature are defined via

$$f(\eta) = \frac{\psi}{U_c\delta}, \quad h(\eta) = \frac{T - T_\infty}{T_0(x) - T_\infty} = \frac{T - T_\infty}{(\nu U_c/g\beta\delta^2)}, \tag{2.5}$$

where $U_c = \nu G^2/4x$ is the local convective velocity and $T_c = (T_0(x) - T_\infty) = \nu U_c/g\beta\delta^2$ is the local excess temperature at the centreline of the plume. With the assumption of power-law variation of T_c ($\sim x^{-3/5}$), the similarity equations can be obtained as

$$f''' + \tfrac{12}{5} ff'' - \tfrac{4}{5} f'^2 + h = 0, \quad h'' + \tfrac{12}{5} Pr(fh)' = 0, \tag{2.6}$$

where the prime denotes differentiation with respect to η, and the related boundary conditions are (Gebhart *et al.* 1970): $f(0) = f''(0) = h'(0) = 0$, $h(0) = 1$, $f'(\infty) \to 0$, $h(\infty) \to 0$. These equations have been solved by using the fourth-order Runge–Kutta method with Newton–Raphson correction. The far-field boundary condition was implemented at $\eta = 12$, and the results were checked by using different values of $\eta = 8, 16, 20, 50$. Figure 1 shows the velocity and the temperature profiles for a range of Prandtl numbers. With increasing Pr, the velocity profile flattens across the plume width, and the temperature boundary layer becomes narrower.

3. Linear stability analysis: quasi-parallel approximation

To analyse the stability of a thermal plume, we decompose each dynamical variable into a mean part (base flow) and a small-amplitude perturbation:

$$u(x, y, t) = u(x, y) + \tilde{u}(x, y, t), \quad v(x, y, t) = v(x, y) + \tilde{v}(x, y, t), \tag{3.1}$$

$$T(x, y, t) = T(x, y) + \tilde{T}(x, y, t), \quad p(x, y, t) = p(x, y) + \tilde{p}(x, y, t), \tag{3.2}$$

with the base flow being taken as that given by the similarity solution (2.6) over which the perturbation equations are linearized. The base flow quantities v and the

x-derivatives of u and T are taken as zero in the linearized perturbation equations – this is called the *quasi-parallel* approximation. The perturbations are assumed to be of a form such that their amplitudes depend on the similarity variable η, as does the base flow.

As in the case of the base flow, it is straightforward to show that the perturbation equations can be expressed in terms of a streamfunction: $\tilde{u} = \partial\tilde{\psi}/\partial y$, $\tilde{v} = -\partial\tilde{\psi}/\partial x$. The resulting perturbation equations (not shown) are amenable to normal-mode analysis:

$$(\tilde{\psi}, \tilde{T})(x, \eta, t) = (\tilde{\phi}, \tilde{s})(\eta)\mathrm{e}^{\mathrm{i}(\alpha x - \omega t)}, \tag{3.3}$$

where α and ω are the non-dimensional wavenumber and frequency, respectively, with δ and $\tau = \delta/U_c$ being the reference length and time scales. The amplitudes for the perturbation stream function and temperature are made dimensionless via $\phi = \tilde{\phi}/U_c\delta$ and $s = \tilde{s}/T_c$. Substituting the normal-mode decomposition (3.3) into the linearized perturbation equations, the coupled Orr–Sommerfeld stability equations are obtained:

$$(\phi'''' - 2\alpha^2\phi'' + \alpha^4\phi + s') = \mathrm{i}\alpha G\left[\left(f' - \frac{\omega}{\alpha}\right)(\phi'' - \alpha^2\phi) - f'''\phi\right], \tag{3.4}$$

$$s'' - \alpha^2 s = \mathrm{i}\alpha Pr G\left[\left(f' - \frac{\omega}{\alpha}\right)s - h'\phi\right]. \tag{3.5}$$

The boundary conditions on $\phi(\eta)$ and $s(\eta)$ are:

$$\phi(\pm\infty) = \phi'(\pm\infty) = s(\pm\infty) = 0. \tag{3.6}$$

3.1. *Varicose and sinuous modes*

For varicose modes, both the velocity and temperatures are symmetric about the mid-plane ($\eta = 0$) which can be translated into following conditions on ϕ and s:

$$\phi(0) = \phi''(0) = s'(0) = 0, \tag{3.7}$$

whereas for sinuous modes, both the velocity and temperatures are asymmetric about the mid-plane ($\eta = 0$) for which the conditions on ϕ and s are:

$$\phi'(0) = \phi'''(0) = s(0) = 0. \tag{3.8}$$

It is known that the thermal plumes are more unstable to sinuous modes (Pera & Gebhart 1971) which has been confirmed in our study. Hence, all results are presented only for sinuous perturbations (3.8).

3.2. *Generalized eigenvalue problem and numerical method*

The linear stability equations, (3.4)–(3.5), along with boundary conditions (3.6) and (3.8), constitute a generalized eigenvalue problem:

$$\boldsymbol{A\Phi} = \lambda\boldsymbol{B\Phi}. \tag{3.9}$$

For the temporal stability analysis, $\lambda = \omega$ is the eigenvalue, $\boldsymbol{\Phi} = (\phi, s)^T$ is the eigenfunction and $\boldsymbol{A}$ and $\boldsymbol{B}$ are 2×2 matrix differential operators whose elements can be easily obtained from (3.4)–(3.5). For the spatial stability analysis, the spatial eigenvalue $\lambda = \alpha$ appears nonlinearly in (3.4)–(3.5) which are subsequently transformed into a linear problem in wavenumber (α) by using the 'companion-matrix' method (Bridges & Morris 1984). For this case, $\Phi = (\alpha^3\phi, \alpha^2\phi, \alpha\phi, \phi, \alpha s, s)^T$ is the eigenfunction and $\boldsymbol{A}$ and $\boldsymbol{B}$ are 6×6 matrix differential operators; the non-zero elements of $\boldsymbol{A}$ are (with $D = \mathrm{d}/\mathrm{d}\eta$): $A_{11} = -\mathrm{i}Gf'$, $A_{12} = \mathrm{i}\omega G + 2D^2$, $A_{13} = \mathrm{i}Gf'D^2 - \mathrm{i}Gf'''$, $A_{14} = -D^4 - \mathrm{i}\omega GD^2$, $A_{16} = -D$, $A_{53} = \mathrm{i}PrGh'$, $A_{55} = -\mathrm{i}PrGf'$, $A_{56} = D^2 + \mathrm{i}\omega PrG$, $A_{21} = 1 = A_{32} = A_{43} = A_{65}$, and $\boldsymbol{B}$ is an unit diagonal operator.

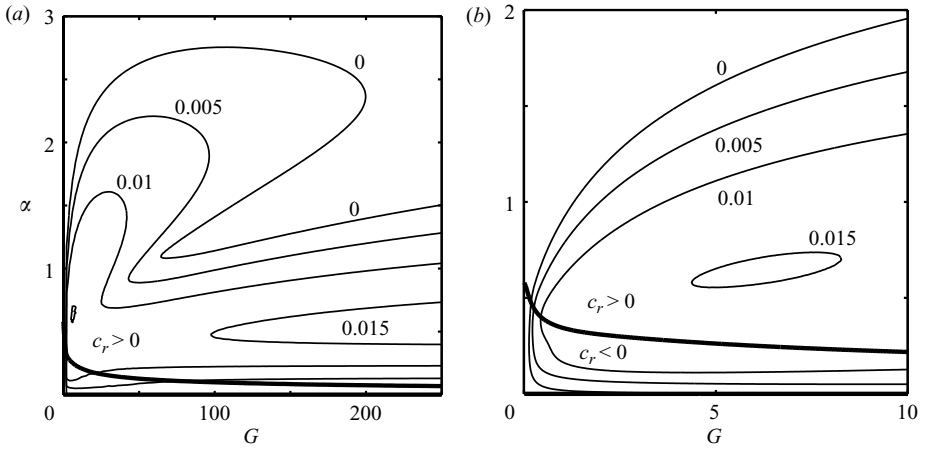

FIGURE 2. For the temporal analysis, the stability diagrams in the (α, G)-plane at $Pr = 200$; (b) is the enlarged part of low-G region.

For the temporal stability, the wavenumber, α, is real and the frequency, $\omega = \omega_r + \mathrm{i}\omega_i$, is complex, with ω_i being the 'temporal' growth/decay rate of the perturbation. For the spatial stability, the frequency, ω, is real and the wavenumber, $\alpha = \alpha_r + \mathrm{i}\alpha_i$, is complex, with α_i being the 'spatial' growth/decay rate. In either case, the flow is said to be stable/unstable if ω_i or $-\alpha_i >, < 0$, respectively, and neutrally stable if ω_i or $\alpha_i = 0$.

For both temporal and spatial analyses, the differential eigenvalue problem (3.9) is transformed into an matrix eigenvalue problem by discretizating the related differential operators along the non-periodic η-direction. We have used two numerical methods for discretization (Malik 1990): (i) the finite-difference method with second-order accuracy; (ii) the Chebyshev spectral collocation method. The resulting matrix-eigenvalue problem has been solved by the QZ-algorithm of Matlab. The growth rate and the phase speed of the least stable mode, obtained from finite-difference and spectral methods, were compared for a few test cases with a different number of grid/collocation points ($N = 101$ and 151). We found that both the growth rate and the phase speed agreed up to the third decimal place for two methods. Moreover, from a comparison with published literature, we found that our neutral stability curve for air ($Pr = 0.7$) agrees well with that of Pera & Gebhart (1971).

4. Results and discussion

We have carried out both temporal and spatial stability analyses of a thermal plume, and most of the results are presented for the temporal case (except in figure 3).

4.1. *Results for various Prandtl numbers*

Figure 2(a) displays a typical stability diagram in the (α, G)-plane at high Prandtl numbers ($Pr = 200$) for the temporal stability analysis; figure 2(b) is the zoomed part of the low-G region of figure 2(a). In each panel, the neutral contour ($\omega_i = 0$) is marked by '0', and the flow is unstable inside it (see the positive growth rate contours) and stable outside. There are two distinct unstable zones: (a) one at low wavenumbers (α) that spans the whole range of Grashof number ($G > G_{cr}$), and (b) the other at relatively higher wavenumbers that spans a limited range of G. Figure 2(b) suggests that there is a minimum value of G below which the plume is stable.

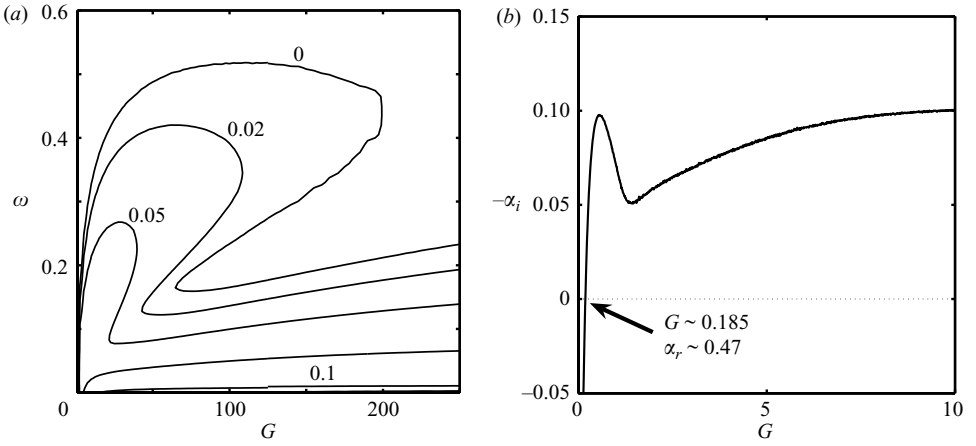

FIGURE 3. For the spatial analysis, (*a*) the stability diagram in the (ω, G)-plane at $Pr = 200$; (*b*) the variation of spatial growth-rate $(-\alpha_i)$ with G for $\omega = 0$.

The thick line in figure 2(*a*, *b*) demarcates the regions of downstream-propagating (phase speed, $c_r = \omega_r/\alpha > 0$) and upstream-propagating ($c_r < 0$) modes in the (α, G)-plane. The origin of such upstream-propagating modes (at low α) remains unclear to us at present. We have checked that the locus of the $(c_r = 0)$-line in the (α, G)-plane does not change by increasing the size of the computational domain from $\eta = 12$ to $\eta = 100$ or by increasing the number of collocation points. We should point out that the possibility of having upstream-propagating modes in a plane thermal plume (which exist for any Pr at very small values of α) has not been mentioned in previous works (Pera & Gebhart 1971; Hieber & Nash 1975; Wakitani 1985). Such modes might be analogous to certain backward-propagating modes in the Ekman boundary layer (Lilly 1966) – this issue is relegated to a future study.

Figure 3(*a*) displays the analogue of figure 2(*a*) in the (ω, G)-plane for the spatial stability analysis. As expected, the stability diagram in the (ω, G)-plane also contains two unstable loops which are analogues of the two loops of the temporal case (figure 2*a*). Focusing on the zero-frequency modes ($\omega = 0$) in figure 3(*a*), we plot the variation of the spatial growth rate of the least-stable mode $(-\alpha_i)$ with G in figure 3(*b*). It is seen that the flow is unstable to $\omega = 0$ modes beyond a minimum Grashof number, $G \sim 0.185$, for $Pr = 200$, and the corresponding real wavenumber is $\alpha_r \sim 0.47$. This critical point $(G, \alpha_r) = (0.185, 0.47)$ from the spatial analysis matches exactly with the intersection point between the neutral curve and the locus of $c_r = 0$ modes in figure 2(*b*) for the temporal analysis. This result establishes that the upstream-propagating modes ($c_r < 0$) for the temporal case are not an artefact of the numerical method.

Hereinafter, we present results only for temporal stability. Focusing on figure 2(*a*), we show the variations of the growth rate and phase speed of the least stable mode with wavenumber in figures 4(*a*) and 4(*b*) for $G = 50$ and $G = 100$, respectively. Two humps in each growth-rate curve correspond to two unstable loops in figure 2(*a*), and the second hump is referred to as a *new mode* since it does not have an analogue in low-Pr fluids. The discontinuities in each phase-speed curve correspond to crossing of different modes.

For a range of Prandtl numbers ($Pr = 0.7$, 100, 200 and 500), the stability diagrams, containing the neutral contour ($\omega_i = 0$) along with a few positive growth-rate contours

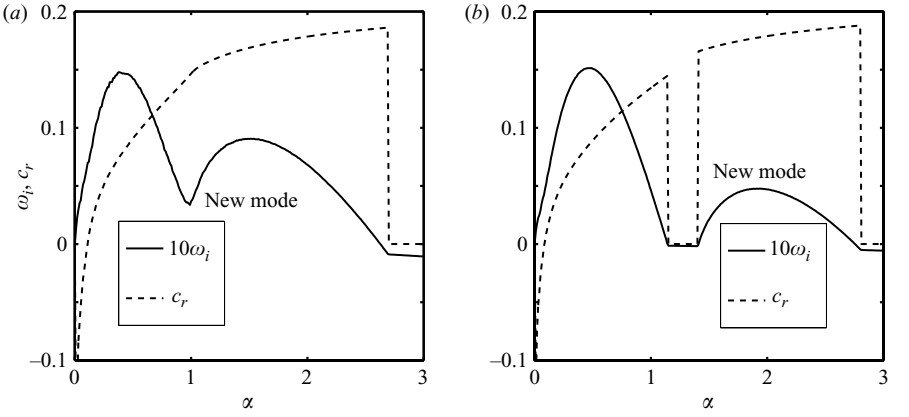

FIGURE 4. Variations of the 'temporal' growth rate (ω_i) and the phase speed ($c_r = \omega_r/\alpha$) of the least stable mode with wavenumber α for (*a*) $G = 50$ and (*b*) $G = 100$, with $Pr = 200$.

($\omega_i > 0$), are compared in the (G, α)-plane in figure 5. For $Pr = 0.7$ (air), the stability diagram has one loop, and the upper branch of the neutral curve is well defined and has an inviscid asymptotic limit: $\alpha = 1.3847$ (Pera & Gebhart 1971). In the limit $G \to \infty$, there exists a range of wave-numbers over which the flow is unstable. At high Prandtl numbers ($Pr > 100$), as in figure 5(*c*), the neutral curve contains a kink, and there is an additional unstable loop at large α and low G. The size of this new unstable loop increases with increasing Prandtl number (see figure 5*d*). As mentioned before, this new unstable loop is referred to as a new mode since it does not appear in low-Pr fluids. Comparing the growth rate contours for different Pr in figure 5, we find that the growth rate of the least stable mode decreases with increasing Prandtl number, even though the size of the unstable zone in the (α, G)-plane increases in the same limit. The thick solid contour in each part of figure 5 is explained in the next section.

Now we suggest a possible experiment to realize this new instability mode. Suppose a laminar plume is disturbed by a small-amplitude sinusoidal excitation of the source with a specified frequency, $f = \omega/2\pi$ (the temperature at the source is constant such that $G = 100$, say, in figure 3*a*). For small enough f, the plume will show a wavy instability according to the lower instability loop in figure 3(*a*), however, for relatively larger f, the plume is unstable to our new instability loop and there is a window of frequencies between two instability modes over which the plume remains stable. It would be interesting to verify this transition scenario at a given Grashof number, 'unstable→stable→unstable' with increasing frequency, in experiments of high Pr-fluids.

4.2. *Origin of the new instability loop: coupling of hydrodynamic and thermal fluctuations*

To shed light on the origin of the new instability loop at high Pr, here we assume that the velocity and the temperature perturbations are decoupled from each other. The full set of stability equations, (3.4)–(3.5), can be made independent from each other by dropping s' and $h'\phi$ from (3.4) and (3.5), respectively. These two sets of equations can now be solved separately to determine the least stable eigenvalue – we have verified that the least stable mode belongs to the Orr–Sommerfeld equation (i.e. a purely hydrodynamic mode, equation (3.4)), and the energy equation (3.5) always yields a stable mode.

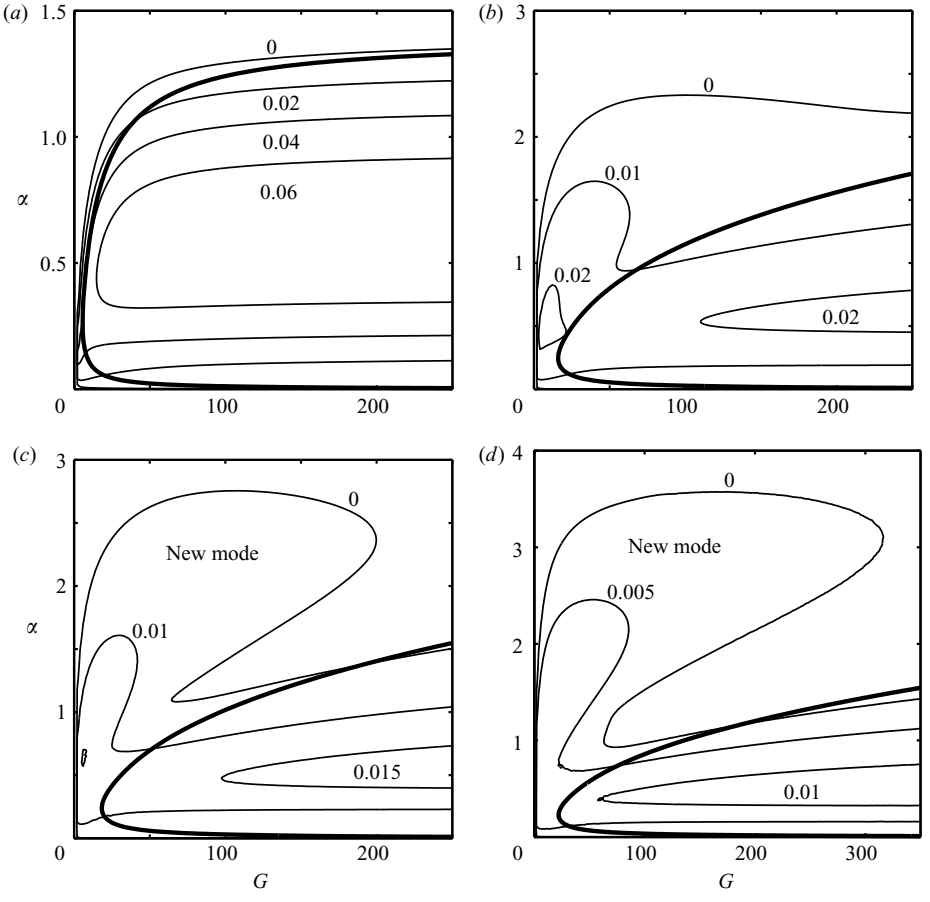

FIGURE 5. Stability diagrams at various Prandtl numbers: (*a*) $Pr = 0.7$; (*b*) $Pr = 100$; (*c*) $Pr = 200$; (*d*) $Pr = 500$. The thick line in each part corresponds to the neutral contour for 'uncoupled' stability equations (see § 4.2 for a related explanation).

For the uncoupled perturbations, the neutral stability curve for each Pr is superimposed as a thick solid contour in figure 5. (The flow is unstable inside the thick contour and stable outside.) A comparison of the thick line in each part with the corresponding neutral contour of coupled stability equations (denoted by the thin curve 0) clearly reveals that the coupling between the hydrodynamic and the thermal disturbance equations is responsible for the origin of our new instability mode at high Pr. The lower parts of the instability loops in figure 5 (*c*, *d*) closely follow the instability loop of the 'uncoupled' Orr–Sommerfeld equation, and are, therefore, purely hydrodynamic in origin.

It is clear that the coupling terms in the stability equations (3.4)–(3.5) are responsible for the appearance of the additional instability loop at high Prandtl numbers, and solving the uncoupled perturbation equations would lead to incorrect results. The importance of this coupling between hydrodynamic and thermal perturbations at high Pr can be understood because the gradient of the base-flow temperature, h', (which appears in the energy perturbation equation) increases with Prandtl number: $h'(\eta) \sim Pr\, f(\eta) h(\eta) \sim Pr^{\epsilon}$, with $0 < \epsilon < 1$, and hence cannot be neglected at large Pr.

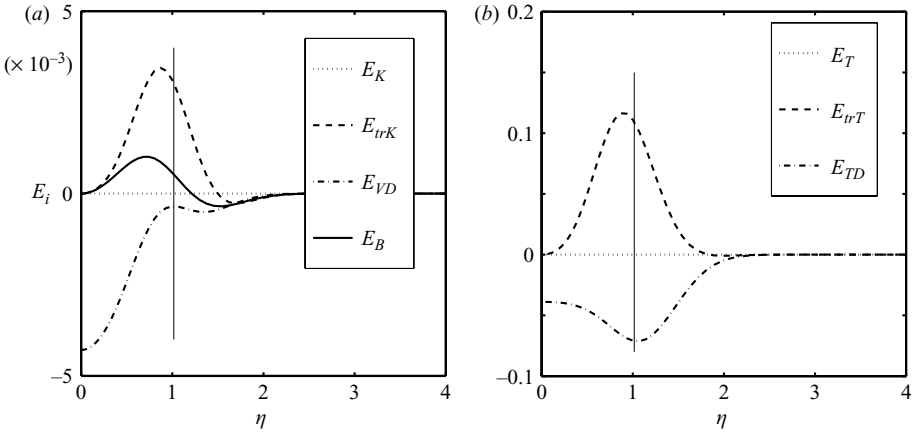

FIGURE 6. Distributions of (*a*) kinetic and (*b*) thermal energies across the plume width for $Pr = 0.7$ (air), $G = 100$, $\alpha = 1.2923$. The vertical line indicates the location of the critical layer.

(From an order-of-magnitude analysis of the pertinent boundary-layer equations, we find $\epsilon = 1/2$.)

4.3. *Analysis of perturbation energy: the instability mechanism*

Lastly, to understand the underlying instability mechanism, we analyse different components of perturbation energy. The time-evolution equations of perturbation kinetic energy and thermal energy are obtained from (3.4)–(3.5) by multiplying them with the corresponding complex conjugate quantity $\phi^{\dagger}$ and $s^{\dagger}$, respectively, and integrating them from $\eta = 0$ to $\eta = \infty$. Considering the real parts, the resulting evolution equations boil down to (Nachtsheim 1963; Gill & Davey 1969)

$$\frac{\mathrm{d}\mathscr{E}_K}{\mathrm{d}t} \equiv \omega_i \int_0^{\infty} e_K \mathrm{d}\eta = \int_0^{\infty} e_{trK} \mathrm{d}\eta + \int_0^{\infty} e_{VD} \mathrm{d}\eta + \int_0^{\infty} e_B \mathrm{d}\eta, \tag{4.1}$$

$$\frac{\mathrm{d}\mathscr{E}_T}{\mathrm{d}t} \equiv \omega_i \int_0^{\infty} e_T \mathrm{d}\eta = \int_0^{\infty} e_{trT} \mathrm{d}\eta + \int_0^{\infty} e_{TD} \mathrm{d}\eta, \tag{4.2}$$

where

$$e_K = (|\phi'|^2 + \alpha^2|\phi|^2), \quad e_{trK} = \alpha f''\left(\phi_r\phi_i' - \phi_r'\phi_i\right), \quad e_{VD} = G^{-1}|\phi'' - \alpha^2\phi|^2,$$
$$e_B = G^{-1}(s_r\phi_r' + s_i\phi_i'),$$
$$e_T = |s|^2, \quad e_{trT} = \alpha h'(\phi_r s_i - \phi_i s_r), \quad e_{TD} = -Pr^{-1}G^{-1}(|s'|^2 + \alpha^2|s|^2),$$

and the suffixes r and i denote the real and imaginary parts, respectively. For hydrodynamic fluctuations, $\mathrm{d}\mathscr{E}_K/\mathrm{d}t$ represents the rate of change of perturbation kinetic energy, $E_{trK} = \int e_{trK}$ the rate of transfer of kinetic energy from the mean flow to perturbations via the Reynolds stress, E_{VD} the rate of viscous dissipation, and E_B the rate of gain of kinetic energy through the buoyancy force. For thermal fluctuations, $\mathrm{d}\mathscr{E}_T/\mathrm{d}t$ is the rate of change of perturbation thermal energy, E_{trT} is the rate of gain of thermal energy from the mean temperature field and E_{TD} is the rate of dissipation of thermal energy.

The variations of different kinetic and thermal energy components across the plume width η are displayed in figures 6 and 7 for $Pr = 0.7$ ($\alpha = 1.2923$) and 200 ($\alpha = 2.74645$), respectively, at $G = 100$. (These two cases correspond to the neutral modes on the upper branch of the neutral contour in figures 5*a* and 5*c*.) In each

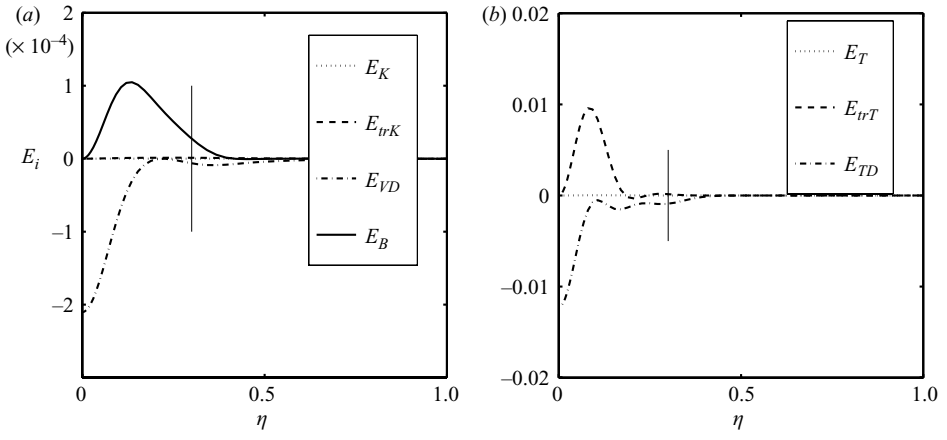

FIGURE 7. Same as figure 6, but for $Pr = 200$, $G = 100$, $\alpha = 2.74645$.

figure, the location of the corresponding critical layer is indicated by the vertical line. Since the instability mode is neutral ($\omega_i = 0$), the net rate of gain of kinetic/thermal energy is $E_K = \omega_i \int e_K \mathrm{d}\eta = 0 = E_T$, denoted by the dotted zero-line in each panel. For $Pr = 0.7$, the kinetic energy gained by the perturbation mainly comes from the Reynold's stress term (E_{trK}) and a small amount is contributed from the perturbation buoyancy force (E_B); the maximum amount of energy is dissipated at the centreline ($\eta = 0$) by viscous forces (E_{VD}). With increasing Pr, the rate of gain of kinetic energy by Reynolds stress becomes progressively smaller, and the buoyancy force (E_B) takes over as the main source of perturbation kinetic energy (see figure 7*a* at $Pr = 200$) which balances the energy lost due to viscous dissipation. We conclude that at high Pr, the contribution from the Reynold's stress term is negligible compared to the gain in kinetic energy by buoyancy force which drives instability.

5. Conclusions

Based on a quasi-parallel stability analysis of a plane thermal plume, we have uncovered a new instability loop at high Prandtl numbers. The origin of this new mode is shown to be tied to the coupling between the hydrodynamic and thermal fluctuations. The importance of this coupling is tied to the increasing magnitude of the base-state temperature gradient with increasing Prandtl number. It is shown that the perturbation kinetic energy gained from the buoyancy force drives this instability at high Pr. The underlying instability mechanism differs from the well-known hydrodynamic instability mechanism for which the perturbation energy is gained from the mean flow via the Reynolds stress. In future, it would be interesting to analyse the effects of non-parallel corrections as well as the temperature-dependent transport coefficients on our new instability loop.

We acknowledge financial support from two grants (DRDO/RN/4124 and PC/EMU/MA/35). M. A. would like to thank Professor Vijay Arakeri for motivating this research.

REFERENCES

BATCHELOR, G. K. 1954 Heat convection and buoyancy effects in fluids. *Q. J. R. Met. Soc.* **80**, 339–359.

Bridges, T. J. & Morris, P. J. 1984 Differential eigenvalue problems in which the parameter appears nonlinearly. *J. Comput. Phys.* **55**, 437–460.

Fujii, T. 1963 Theory of the steady laminar natural convection above a horizontal line heat source and a point heat source. *Intl J. Heat Mass Transfer* **6**, 597–606.

Gebhart, B., Pera, L. & Schorr, A. 1970 Steady laminar natural convection plumes above a horizontal line heat source. *Intl J. Heat Mass Transfer* **13**, 161–171.

Gebhart, B., Jaluria, J., Mahajan, R. L. & Sammakia, B. 1988 *Buoyancy Induced Flows and Transport*. Hemisphere.

Gill, A. E. & Davey, A. 1969 Instabilities of a buoyancy-driven system. *J. Fluid Mech.* **35**, 775–798.

Grossmann, S. & Lohse, D. 2000 Scaling in thermal convection: a unifying theory. *J. Fluid Mech.* **407**, 27–56.

Hieber, C. A. & Nash, E. J. 1975 Natural convection above a line heat source: higher order effects and stability. *Intl J. Heat Mass Transfer* **18**, 1473–1479.

Kaminski, E. & Jaupart, C. 2003 Laminar starting plumes in high-Prandtl-number fluids. *J. Fluid Mech.* **478**, 287–298.

Lilly, K. L. 1966 On the instability of Ekman boundary flow. *J. Atmos. Sci.* **21**, 481–494.

Lister, J. R. 1987 Long-wavelength instability of a line plume. *J. Fluid Mech.* **175**, 571–591.

Majumder, C. A. H., Yuen, D. A. & Vincent, A. P. 2004 Four dynamical regimes for a starting plume model. *Phys. Fluids* **16**, 1516–1531.

Malik, M. R. 1990 Numerical methods for boundary layer stability. *J. Comput. Phys.* **86**, 376–413.

Nachtsheim, P. R. 1963 *Stability of free convection boundary layers. NASA TN* D-2089.

Pera, L. & Gebhart, B. 1971 On the stability of laminar plumes: some numerical solutions and experiments. *Intl J. Heat Mass Transfer* **14**, 975–984.

Riley, N. 1974 Free convection from a horizontal line source of heat. *Z. Angew. Math. Phys.* **25**, 817–828.

Wakitani, S. 1985 Non-parallel flow instability of a two dimensional buoyant plume. *J. Fluid Mech.* **159**, 241–258.

Wang, X. 2004 Infinite Prandtl number limit of Rayleigh–Bénard convection. *Commun. Pure Appl. Maths.* **57**, 1265–1282.

Worster, M. G. 1985 Asymptotic analysis of a high Prandtl number axisymmetric plume. *Stud. Appl. Maths.* **159**, 241–258.